Discover Applied Sciences

RESEARCH Open Access

Enhanced electrochemical performance of carbonized porous organic polymers towards supercapacitor application

Abdul Kareem[1,2], Muhammad Faheem Maqsood[3], Feroz A. Sofi[1], Mohammad H. Al-Sayah[1,2,3*] and Oussama M. El-Kadri[1,2,3*]

*Correspondence:
Mohammad H. Al-Sayah
malsayah@aus.edu
Oussama M. El-Kadri
oelkadri@aus.edu
[1]Materials Research Center, College of Arts and Sciences, American University of Sharjah, PO Box 26666, Sharjah, United Arab Emirates
[2]Department of Biology, Chemistry, and Environmental Sciences, American University of Sharjah, PO Box 26666, Sharjah, United Arab Emirates
[3]Materials Science and Engineering PhD Program, College of Arts and Sciences, American University of Sharjah, PO Box 26666, Sharjah, United Arab Emirates

Abstract

To develop a functional supercapacitor with enhanced electrochemical activity, it is essential to explore electrode materials that exhibit good conductivity and capacitance. This study investigates the development of supercapacitor electrodes based on porous organic polymers (POP-O and POP-S) and their carbonized counterparts (C-POP-O and C-POP-S). The structural transformation from amorphous to partially graphitic carbon material is confirmed by Raman analysis. Field emission scanning electron microscopy (FE-SEM) revealed significant morphological changes, with the carbonized materials exhibiting more defined structures contributing to improved electrochemical performance. Electrochemical tests, including cyclic voltammetry (CV) and galvanostatic charge-discharge (GCD), show that the carbonized form of these materials can significantly increase the current density, specific capacitance, and charge-transfer efficiency. Among the synthesized materials, C-POP-O exhibits the highest specific capacitance of 47.43 F g^{-1} at 1 A g^{-1} with excellent GCD cyclic stability, by retaining 96% capacitance from its starting capacitance after 5000 GCD cycles, indicating its potential as a high-performance electrode. These findings highlight the potential of carbonized porous organic polymers, particularly C-POP-O, as high-performance electrodes for next-generation supercapacitors.

Keywords Supercapacitor electrodes, Porous organic polymers (POP), Carbonized materials, Electrochemical performance, Energy storage materials

1 Introduction

With the growing global energy demand driven by population growth, researchers are intensifying their efforts to develop efficient, cost-effective, and environmentally friendly materials [1, 2]. By exploring novel materials and technologies, scientists are working to reduce the dependence on fossil fuels and mitigate the environmental impact of energy production, ultimately paving the way for a cleaner and more sustainable future [3–5]. These advancements aim to enhance energy conversion processes and create sustainable storage systems to meet future energy needs [6–8]. Consequently, energy storage

technologies with clean and renewable energy solutions are gaining widespread global attention. Innovations in renewable energy, next-generation batteries, and supercapacitors are proving essential for achieving long-term energy sustainability [9, 10].

Supercapacitors (SCs), which act as intermediates between traditional capacitors and batteries, have emerged as vital tools in energy storage [11, 12]. Especially, Electrochemical capacitors (ECs) are of great interest due to their exceptional power density and energy density. The electrochemical performance of ECs is heavily influenced by the selection of electrode materials, which fall into three primary categories: conductive polymers, carbon-based materials, and transition metal oxides or nitrides [13, 14]. Transition metal oxides are limited owing to their corrosive nature in harsh conditions [15, 16]. Carbon-based materials, such as porous organic polymers (POPs), carbon nanotubes (CNTs), graphene, and porous carbon, are especially valued for supercapacitor applications due to their structural tunability, thermal stability, and catalytic properties [17, 18].

Specifically, porous organic polymers (POPs), have attracted attention owing to their high porosity, low density, and unique properties [19–21]. The electrochemical properties of these materials, such as conductivity, surface area, and chemical reactivity, can be enhanced by incorporating certain chemical functionalities that can modify or enhance the properties of the materials [22, 23]. Such systems have been demonstrated to have high electrochemical performance as supercapacitor electrode materials. For example, Hu et al. synthesized redox-active 2D POPs (Tp-AT-POP) that exhibited a specific capacitance and excellent cycling stability [24]. Meanwhile, Xu et al. reported a hybrid composite of POPs and reduced graphene oxide (rGO) for improved supercapacitor activity [25]. On the other hand, combining the POPs with electrochemically active material further enhances their properties [26, 27]. For example, a novel POP with hydroxyquinoline, as an electrochemically active unit, exhibited high specific capacitance, excellent rate capability and good cycling stability [28].

To develop electrochemical double-layer capacitors (EDLCs) with high energy and power density, carbon-based materials derived through chemical or physical methods are essential due to their high surface area and high conductivity [29]. POP-derived Carbon material has various advantages (like high pore structure and low density) over traditional biomass-derived or activated carbon materials. More significantly, porous carbon generated from POPs creates a new avenue for the manufacture and utilization of carbon-based materials for energy storage. Carbonization of POPs for preparing carbon materials can be a suitable approach for energy conversion and storage devices. These obtained carbon materials can acquire high porosity inherited from POPs and the graphitic carbon structure can enhance the conductivity and stability of the material [30]. Notably, because of their diverse structural units and distinct pore architectures, POPs have emerged as one of the most promising precursors to produce advanced carbonaceous materials [31, 32]. For example, Liang et al. reported a series of POPs using different carbon precursors like biphenyl dichlorobenzene, pyrene and 1, 3, 5-triphenyl benzene. The obtained porous carbon exhibited a high specific surface area of 2668 m^2 g^{-1} and a pore diameter of 2.3 nm [33].

Motivated by these studies, in this work, we investigated the potential of supercapacitor electrodes using our recently reported porous organic polymers (POP-O and POP-S) [34] and their carbonized forms (C-POP-O and C-POP-S). A pyrolysis method was

used to obtain the carbonized form of these POPs. Raman analysis confirms the successful formation of graphitic carbon upon pyrolysis and FE-SEM images revealed that the carbonization process can improve the structural order. Electrochemical characterization, including cyclic voltammetry (CV) and galvanostatic charge-discharge (GCD), exhibited a significant increase in capacitance and current density for carbonized materials (C-POP-O and C-POP-S) over the corresponding POPs. Among these materials, C-POP-O exhibited the highest electrochemical activity towards supercapacitor application with a high specific capacitance value of 47.43 F g^{-1} at the current density of 1 A g^{-1}. Besides, both C-POP-O and C-POP-S demonstrated excellent stability during 5000 GCD cycles at 2 A g^{-1}; they retained 96% and 89% efficiency, respectively, after 5000 GCD cycles compared to the initial cycle.

2 Experimental work

2.1 Materials

All reagents used in this study, including 2-furaldehyde (≥ 98%), 2-thiophenecarboxaldehyde (≥ 99%), dimethyl sulfoxide (DMSO) (≥ 99.7%), tetrahydrofuran (THF) (≥ 99.9%), N-Methyl-2-Pyrrolidone (NMP) (≥ 99%), polyvinylidene fluoride (PVDF), acetone, methanol, dichloromethane, chloroform, hydrazine hydrate, sodium chromate, potassium hydroxide (KOH) (≥ 85%) pellets and carbon cloth were sourced from Sigma-Aldrich and used as obtained without further purification. All the aqua solutions were prepared using deionized water (DI water). 9,10-bis-(4,6-diamino-S-triazin-2-yl) benzene (BATB), NRAPOP-O, and NRAPOP-S were synthesized following a previously published study [34]. In this study, NRAPOP-O and NRAPOP-S are referred to as POP-O and POP-S, respectively, for simplicity.

2.2 Carbonization of POP-O and POP-S

For the carbonization process, the purified samples of both POP-S and POP-O were placed in a quartz boat and subjected to heating at 500 °C under an Argon atmosphere, following a three-step program in a programmable furnace. The first step involved holding the samples at room temperature for 10 min, then gradually increasing to 500 °C with a heating rate of 10 °C per minute. In the final step, the temperature was raised to 500 °C, where the samples were maintained for two hours (Scheme 1). During the pyrolysis process of POPs at 500 °C, the obtained carbon materials retain the polymeric framework, while heteroatoms (O, S, N) are largely removed, leaving behind partially graphitic carbon frameworks. This transformation increases π-conjugation and conductivity [29–31]. After the carbonization process was complete and the furnace had cooled down to room temperature, the obtained black samples were collected, and the

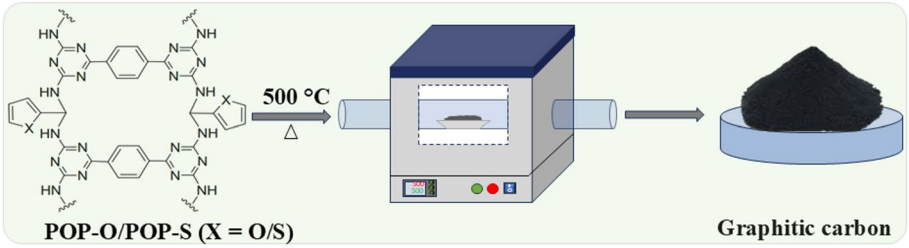

Scheme 1 Schematic presentation of the carbonization process of POP-O and POP-S

respective weights were recorded. Herein, the carbonized POP-O and POP-S are named C-POP-O and C-POP-S.

2.3 Characterization

Crystallographic data were collected using a Malvern Panalytical X'Pert3 diffractometer by analyzing X-ray diffraction (XRD) patterns with Cu–Kα radiation over a 10° to 80° range at room temperature. Raman spectroscopy (Alpha 300 (Witec) confocal Raman microscope) was used to confirm the degree of disorder in the carbonized materials. The surface morphology and elemental composition of the prepared samples were examined with a field-emission scanning electron microscope (FE-SEM, TESCAN MAGNA).

2.4 Electrode preparation

To prepare the POP-S, POP-O, and the electrodes of their carbonized powder, started by measuring the weight of the powders. Herein, ~ 90 wt% POP-based materials (POP-S/POP-O/C-POP-S/C-POP-O) were mixed with 10 wt% of polyvinylidene fluoride (PVDF) and a few drops of N-Methyl-2-Pyrrolidone (NMP). Further, the mixture was ground using a mortar and pestle until a homogeneous slurry was formed. This prepared slurry was evenly applied over a piece of carbon cloth (1×1 cm^2), ensuring a uniform distribution. After this, the prepared electrode was dried in a hot air oven overnight. The mass loading of active material was obtained ~ 3 mg cm^{-2}, measured by taking the weight difference of carbon cloth before coating and after drying.

2.5 Electrochemical characterization

Electrochemical analysis was conducted using a CHI 660E electrochemical workstation from CH Instruments Inc. (Austin, TX) with a three-electrode setup in a 1 M KOH electrolyte. Prepared electrodes act as the working electrode, with a platinum (Pt) wire as the counter electrode and Hg/HgO as the reference electrode. In order to activate and stabilize the electrode, 100 Cyclic voltammetry (CV) cycles were performed in the potential window from 0 to 0.6 V vs. Hg/HgO at 100 mV s^{-1}. Further, CV cycles were recorded at various scan rates within a 0 to 0.6 V potential range, while galvanostatic charge–discharge (GCD) tests were performed at different current densities (1, 2, 3, and 4 A g^{-1}) in a potential range from 0 to 0.6 V, to calculate the specific capacitance. The specific capacitance from GCD was calculated using the linear approximation Eq. (1) [35].

$$C_{sp} = \frac{I \, \Delta t}{m \, \Delta V} \tag{1}$$

where I is an applied current (A), Δt is a discharge time (s) of the GCD curve, ΔV is the potential window (V), and m is the active mass loading (g) on the working electrode [36, 37]. This method assumes a near-linear discharge profile, which is typical for carbon-based electrodes. The electrochemical impedance spectroscopy (EIS) data were collected at open-circuit potential (OCP) in the frequency range from 100 kHz to 0.1 Hz.

3 Results and discussion

3.1 Structural and morphological characterization

The carbon materials were synthesized using the pyrolysis method as shown in Scheme 1, where POP-O and POP-S were heated at 500 °C to obtain C-POP-O and C-POP-S. All

the prepared materials, including POP-S, POP-O, C-POP-S, and C-POP-O, were characterized using XRD and Raman. Figure 1A displays the XRD patterns for both POP-S (black curve) and POP-O (red curve), which exhibit a broad peak around 17–25° (2θ), indicating their amorphous or poorly crystalline nature, characteristic of disordered porous organic polymers. POP-O shows a slightly broader peak compared to POP-S, suggesting a marginally lower degree of structural order than POP-S. After carbonization, the C-POP-S (Fig. 1A, blue curve) and C-POP-O (Fig. 1A, green curve) samples display broad peaks that shift slightly to a higher angle, centering around 20–27° (2θ), which is indicative of the formation of short-range graphitic domains. This peak shift, along with the narrower and more pronounced profiles, suggests the formation of graphitic carbon [38]. Despite the shift and improved structural uniformity, sharp, well-defined peaks are absent, indicating that full crystallinity has not been achieved.

Additionally, to verify the presence of graphitic carbon, all the synthesized materials underwent characterization via Raman spectroscopy. The flat curves of POP-S (Fig. 1B, black curve) and POP-O (Fig. 1B, red curve) indicate that neither shows a signal in the Raman spectra, which suggests the absence of graphitic carbon. In contrast, C-POP-S (Fig. 1B, blue curve) and C-POP-O (Fig. 1B, green curve) exhibit two distinct peaks at 1342 and 1580 cm^{-1}, corresponding to the D band and G band, respectively. These bands confirm the successful formation of graphitic carbon following pyrolysis. C-POP-O displays significantly more intense peaks compared to C-POP-S, indicating a higher degree of carbon formation in C-POP-O.

The FE-SEM investigation reveals significant changes in the morphology of POP-S and POP-O, after carbonization (C-POP-S and C-POP-O), which align closely with the structural insights provided by the XRD and Raman results. The POP-S (Fig. S1A, B, C) and POP-O (Fig. S1D, E, F) have a rough, granular surface with uneven particle distribution, indicating a disordered structure. These surface characteristics correlate with the XRD patterns, where both materials show broad peaks indicating their amorphous or poorly crystalline nature [39]. After carbonization, C-POP-S exhibits a clear agglomerated layered fragments morphology as shown in Fig. 2A, B, C. Meanwhile, C-POP-O develops layered fragments, suggesting a more ordered, graphitic-like structure depicted in Fig. 2D, E, F. After pyrolysis, no major changes occur in morphology. However, to show the minor changes that occurred after pyrolysis, the SEM images were captured at the same scale. It can be observed from Fig. S1F (POP-O) and Fig. 2F (C-POP-O) at 500 nm that C-POP-O is in a layered fragments-like morphology and POP-O is more

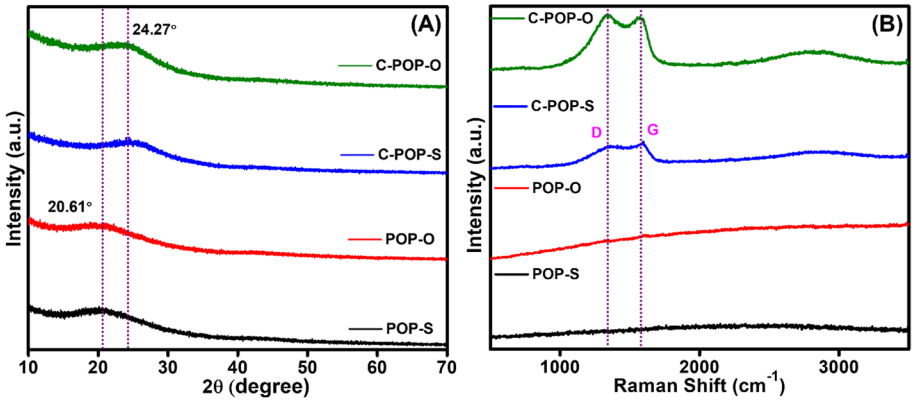

Fig. 1 (**A**) XRD patterns and (**B**) Raman spectra of the POP-S, POP-O, C-POP-S, and C-POP-O powders

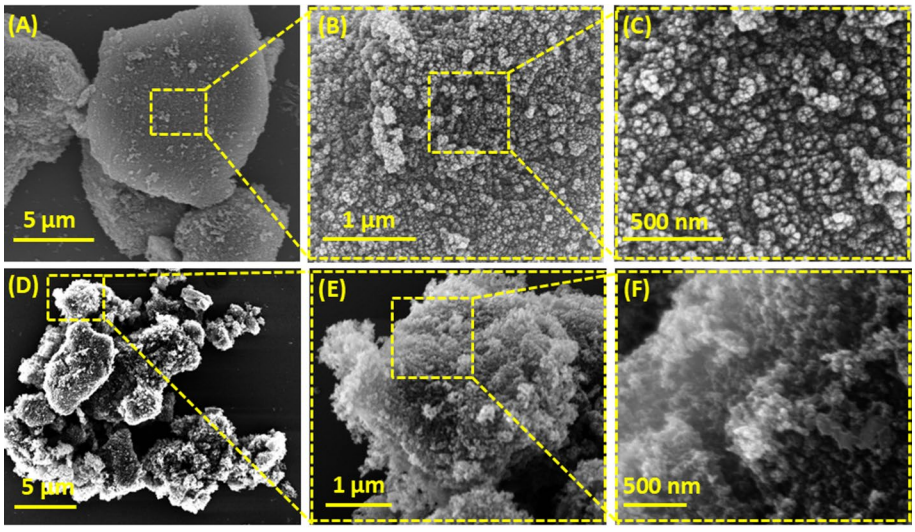

Fig. 2 FE-SEM images of (**A**, **B**, **C**) C-POP-S and (**D**, **E**, **F**) C-POP-O powders

like amorphous. The EDX analysis in Fig. S2 highlights the elemental composition of different samples labeled POP-S, POP-O, and their canonized counterparts, C-POP-S and C-POP-O. In the non-carbonized samples, POP-S shows the presence of carbon (76%), nitrogen (23.4%), and sulfur (0.6%). On the other hand, POP-O contains carbon (70.3%) and smaller amounts of nitrogen (26.6%), oxygen (2.8%) and sulfur (0.3%). After carbonization, the samples (C-POP-S and C-POP-O) show a drastic change in their composition. Both C-POP-S and C-POP-O exhibit 100% carbon content, suggesting that the pyrolysis process successfully carbonized the samples, removing all other detectable elements, including nitrogen, sulfur, and oxygen. This transformation indicates that the pyrolysis process has effectively converted the POP materials into graphitic carbon. Furthermore, the EDX mapping of the carbonized materials confirms the formation of pure carbon and the removal of all other elements (Fig. S3). Thus, the peak shift in XRD and the formation of the D and G band in Raman spectra confirms the formation of graphitic carbon. Further, the sharper XRD peak of C-POP-O compared to C-POP-S and the well-defined D and G bands of C-POP-O compared to C-POP-S confirm that the graphitic carbon formed through C-POP-O is in well order and more crystalline compared to the carbon formed through C-POP-S. The high crystalline carbon materials provide high conductivity and ion diffusion due to their expanded π conjugation. On the other hand, the low crystalline carbon material could not perform well due to broken carbon domains.

3.2 Electrochemical measurements

The electrochemical activity of these materials was investigated in 1 M KOH using a standard three-electrode system. Figure 3 shows the CV curves for all the prepared samples, including POP-S, POP-O, C-POP-S and C-POP-O. Figure 3A exhibits that the POP-S reaches the current density of around 3.87 A g^{-1} at a scan rate of 100 mV s^{-1} within a potential range from 0 to 0.6 V (this current was noted at the potential of 0.6 V). The curves display stable and symmetric capacitive behavior across all scan rates (from 5 mV s^{-1} to 100 mV s^{-1}), indicating high electrochemical reversibility and effective

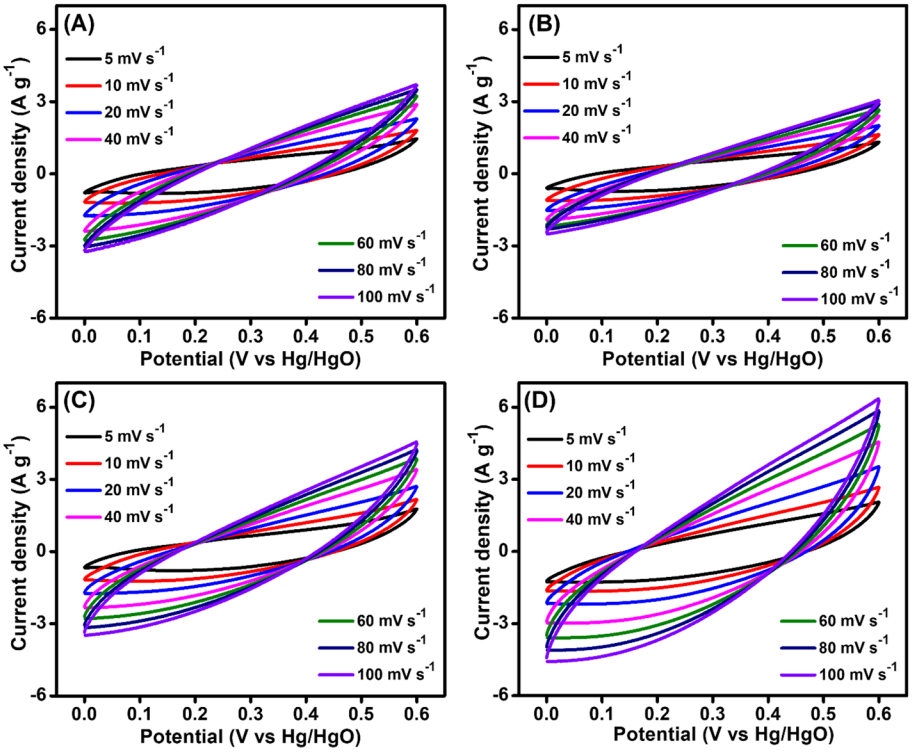

Fig. 3 CV curves of (**A**) POP-S, **B** POP-O, **C** C-POP-S, and **D** C-POP-O based electrodes

charge storage capacity in the POP-S material. Upon the pyrolysis process, the carbonized form of POP-S (C-POP-S) displays a significant increase in current density as shown in Fig. 3C, reaching approximately 4.58 A g^{-1} at 100 mV s^{-1}. This improvement signifies enhanced conductivity and increased capacitance, likely due to structural changes from carbonization. The graphitic carbon shows improved charge transport properties and an increased electrochemically active surface area, enhancing the electrochemical performance of C-POP-S.

On the other hand, POP-O (Fig. 3B) exhibited a current density of 3.08 A g^{-1} at a scan rate of 100 mV s^{-1}. Like POP-S, the CV curves of POP-O maintain stable, symmetric profiles, confirming electrochemical reversibility and effective capacitive behavior. After carbonization, C-POP-O shows a significant boost in current density, it reaches at 6.39 A g^{-1} at 100 mV s^{-1}, which is more than double that of POP-O depicted in Fig. 3D. This considerable enhancement indicates improved conductivity and specific capacitance due to the carbonization process, which introduces better structural organization and additional pathways for ion transport. The carbonized form of POP-O (C-POP-O) displays superior electrochemical activity owing to a well-ordered carbon structure, as shown in the Raman spectrum (Fig. 1B, green curve). In comparison with C-POP-S, C-POP-O exhibited better performance. As can be observed from Fig. 2F that C-POP-O has layered fragments like morphology, due to which a higher area of active material can be exposed to the electrolyte and gives high performance. But, C-POP-S has more agglomerated morphology (Fig. 2C), due to which a limited area gets exposed to the electrolyte, resulting in limited activity.

Similarly, the improved activity of the electrocatalyst can be explained by the electrochemically active surface area (ECSA). The increased ECSA was confirmed using

electrochemical characterization techniques. As can be observed from Fig. 3, a higher capacitive current response was observed for C-POP-O, and a larger capacitive (non-faradaic) current response in the CV curves indicates higher double-layer capacitance (C_{dl}), which correlates with increased electrochemically active surface area (ECSA). C-POP-O shows higher current and area under the curve compared to C-POP-S, which could be due to the availability of a higher electrochemically active surface area of C-POP-O for ion adsorption.

Furthermore, Fig. 4 illustrates the galvanostatic charge-discharge (GCD) profiles for the POP-O, POP-S, C-POP-O and C-POP-S electrodes, at various current densities ranging from 1 A g^{-1} to 4 A g^{-1} within a potential window of 0 to 0.6 V. It can be observed that the carbonized materials display higher discharge time compared to pristine materials, owing to the high charge storage capacity of carbon materials. Among the synthesized materials, C-POP-O exhibited the highest discharge time compared to all other materials at different current densities. This could be due to the formation of well-ordered graphitic carbon through the pyrolysis of POP-O, as it can be observed from the Raman spectrum. The specific capacitance was calculated from GCD for C-POP-O is 47.43 F g^{-1}, which is higher than C-POP-S (43.3 F g^{-1}), POP-S (37.2 F g^{-1}), and POP-O (24.4 F g^{-1}) at 1 A g^{-1}. At a lower current density of 1 A g^{-1}, the discharge duration is greater, indicating that the material operates well under low-stress circumstances. The specific capacitance was calculated at different current densities as compared in Fig. S4. It can be observed that the capacitance decreased with increasing current density. At a lower current density, electrolyte ions have sufficient time to diffuse deeply into the porous structure and access the full electrochemically active surface area of the electrode. As a result, a larger fraction of the surface contributes to charge storage, yielding higher capacitance values. However, at higher scan rate or current density, the ion

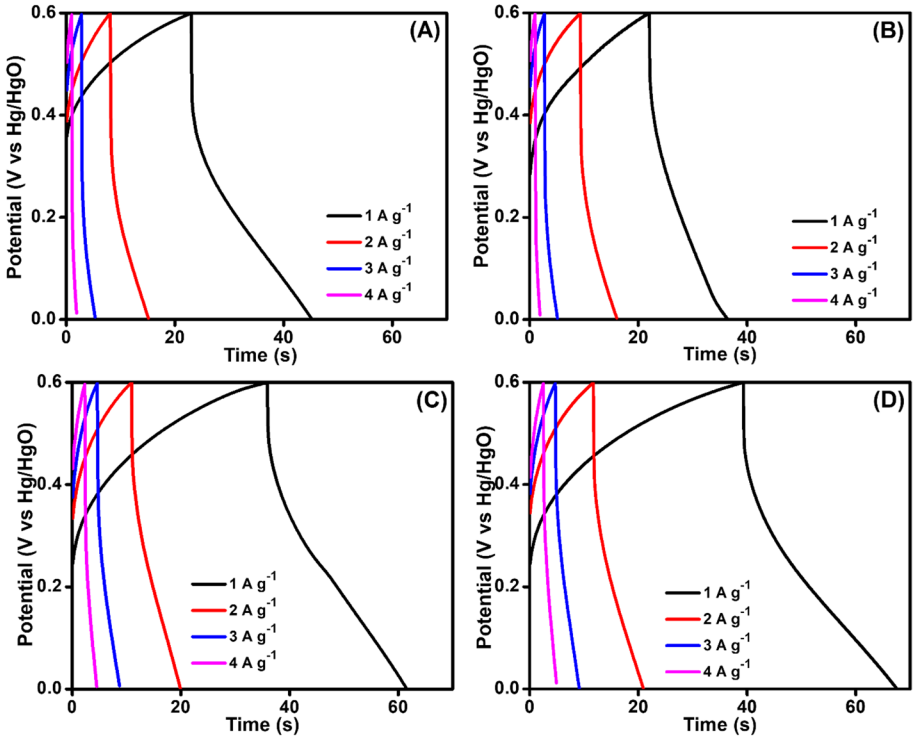

Fig. 4 GCD curves of (**A**) POP-S, **B** POP-O, **C** C-POP-S and **D** C-POP-O based electrodes

Table 1 Comparison of specific capacitance at different current densities

Current density	C-POP-O	C-POP-S	POP-S	POP-O
1 A g^{-1}	47.4 F g^{-1}	43.3 F g^{-1}	37.2 F g^{-1}	25.0 F g^{-1}
2 A g^{-1}	31.3 F g^{-1}	30.0 F g^{-1}	23.3 F g^{-1}	22.7 F g^{-1}
3 A g^{-1}	21.5 F g^{-1}	21.0 F g^{-1}	12.5 F g^{-1}	12.0 F g^{-1}
4 A g^{-1}	16.7 F g^{-1}	15.3 F g^{-1}	6.0 F g^{-1}	6.0 F g^{-1}

Table 2 Performance comparison of carbonized electrodes derived from different sources at 1 Ag^{-1}

Electrode material	Preparation method	Electrolyte	Specific capacitance	Cyclic stability Retention (%)	Ref.
Biomass-derived porous carbon	Carbonization at 600 °C	$EmimBF_4$	21 F g^{-1}	93% after 5000 cycles	[44]
Hemp-derived carbon	Carbonization at 800 °C	1.8 M $TEMABF_4$	41 F g^{-1}	90% after 10,000 cycles	[45]
Capsicum seed-derived carbon	Carbonization at 850 °C	EMIM-TFSI	29 F g^{-1}	91% after 5000 cycles	[46]
POP-derived carbon	Pyrolysis at 700 °C	6 M KOH	162 F g^{-1}	95% after 5000 cycles	[18]
COF-derived porous carbon	Pyrolysis at 800 °C	1 M H_2SO_4	250 F g^{-1}	92% after 10,000 cycles	[22]
POP-derived hierarchical carbon	Iono thermal synthesis + carbonization	1 M KOH	210 F g^{-1}	94% after 8000 cycles	[30]
C-POP-S	Pyrolysis at 500 °C	1 M KOH	43.3 F g^{-1}	89% after 5000 cycles	This study
C-POP-O	Pyrolysis at 500 °C	1 M KOH	47.4 F g^{-1}	96% after 5000 cycles	This study

*1-ethyl-3-methyl imidazolium tetrafluoroborate ($EmimBF_4$), 1-ethyl-3-methylimidazolium bistrifluorosulfonylimide (EMIM-TFSI)

diffusion process becomes kinetically limited. Only the outer and more easily accessible surface sites participate in charge storage, while the inner active sites remain underutilized. This limited accessibility, coupled with increased resistive losses at higher current flow, leads to a reduction in the measured capacitance. Therefore, the observed decrease in capacitance with increasing current density is attributed to the diffusion-controlled insertion [40, 41].

However, when the current density increases, performance decreases considerably, suggesting a limited charge storage capability at higher current densities. Additionally, the specific capacitance values calculated from GCD were also compared in Table 1. Further, the electrochemical performance of C-POP-O is compared with various carbon materials, derived from different sources, at 1 A g^{-1} in Table 2. It can be observed from GCD curves that the discharge capacitance is lower than the charge capacitance, which typically indicates nonlinear behavior in the electrochemical system. At the current density of 1 A g^{-1}, the charging rate is slow and the discharge rate is high, resulting in the low Coulomb efficiency of C-POP-O (72.3%), C-POP-S (72.0%), POP-S (97.2%) and POP-O (68.8%). Further, the coulombic efficiency was calculated for all the samples at different current densities and compared in Fig. S5. The non-linear dependences of voltage on time were attributed to porosity and internal resistance R_{ESR}, which are related to the carbon material structure and the difficult accessibility of fine pores to electrolyte ions [42, 43].

The improved supercapacitor performance can be explained as suggested in Fig. 5. POPs are low-conducting materials with high porosity and upon carbonization, highly

porous and conductive carbon material can be obtained. Owing to low conductivity, less number of ions at the surface of POPs and results in low capacitive behavior. On the other hand, owing to high conductivity, more number of ions occur on the surface of carbonized POP, resulting in high capacitance.

Stability is an important parameter to evaluate the effectiveness of the materials. Hence, to demonstrate the stability of carbonized materials, 5000 GCD cycles were performed at the current density of 2 A g^{-1}. IR drop corrections were carried out throughout 5000 GCD cycles. This IR drop is critical to evaluate the degradation of this electrode. Figure 6A shows the specific capacitance at different numbers of cycles for C-POP-O and C-POP-S. Both of the carbonized materials exhibit excellent stability even after 5000 GCD cycles. C-POP-O retains around 96% efficiency and C-POP-S retains around 89% efficiency after 5000 GCD cycles from the initial cycle. Further to demonstrate the stability of these materials, C-POP-O and C-POP-S have been characterized using SEM analysis after 5000 GCD cycles. Fig. S6 shows the SEM images of C-POP-S and C-POP-O after 5000 GCD cycles. It could be observed from SEM images that the morphology of C-POP-S and C-POP-O is being unchanged even after 5000 GCD cycles and the EDS spectra show the presence of K (45.7%), O (33.5%) and C (20.8%) in C-POP-S and the presence of K (15.7%), O (13.4%) and C (71.0%) in C-POP-O (Fig. S7). The occurrence of K and O could be due to the deposition of KOH on the surface of the electrode. In order to demonstrate the change in conductivity of POP materials after the carbonization process, the EIS analysis was utilized. The Nyquist plots were fitted according to the circuit given in Fig. 6B (inset). Where different elements of the circuit represent different parameters, such as R_s stands for solution resistance or the ohmic resistance of

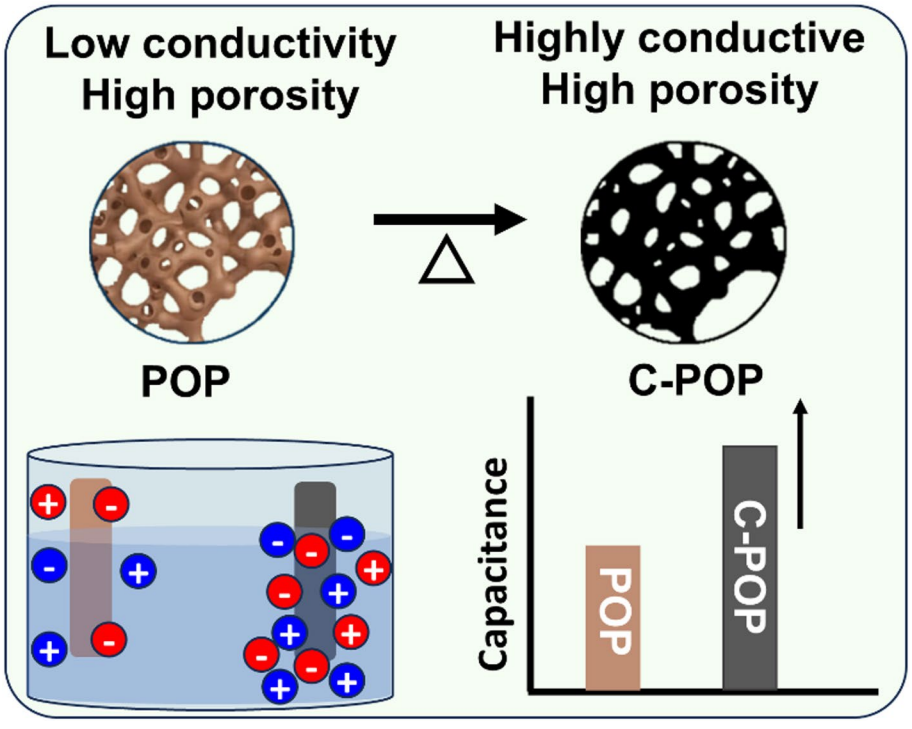

Fig. 5 Schematic explanation of the energy storage capacity of POP and C-POP based on the porosity and conductivity

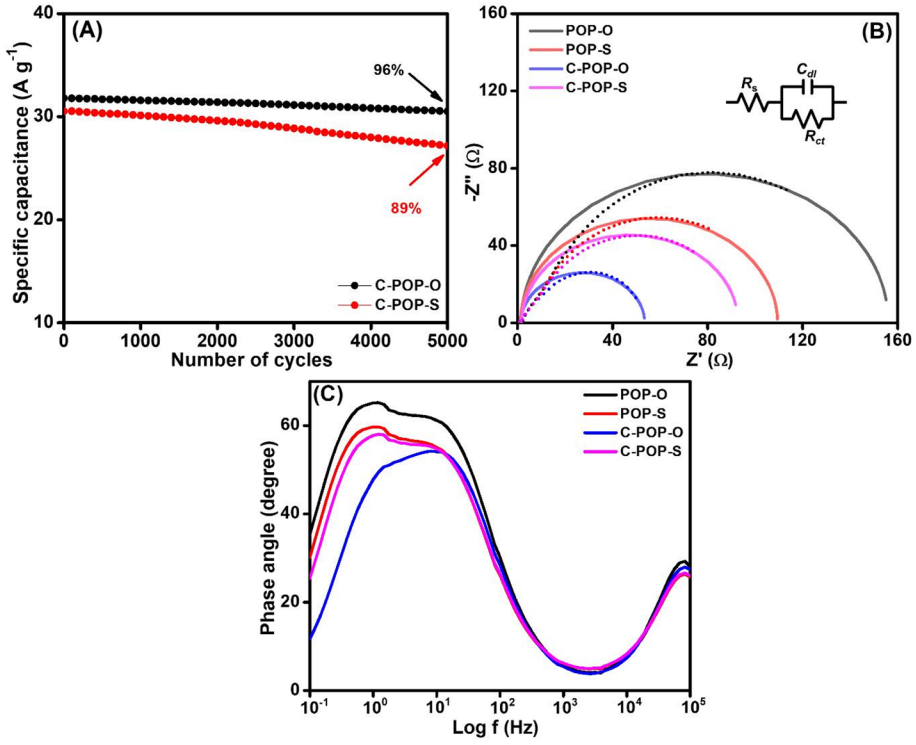

Fig. 6 (**A**) 5000 GCD cycles of C-POP-S and C-POP-O, **B** Nyquist plot; (inset) corresponding circuit and (**C**) Bode phase angle plot of POP-S, POP-O, C-POP-S and C-POP-O

electrolyte between reference and working electrode, which is called the uncompensated resistance. The C_{dl} stands for the electric double layer at the electrode/electrolyte interface and R_{ct} shows the charge transfer resentence of the electrode material. The lower R_{ct} value demonstrates the higher conductivity of a material [47]. Figure 6B shows the Nyquist plot of all the synthesized materials, and the diameter of the semicircle represents the R_{ct} values. C-POP-O exhibits a lower charge transfer resistance value of 52 Ω compared to C-POP-S (92 Ω), POP-S (108 Ω), and POP-O (155 Ω). Furthermore, this bulk resistance (Ω) is converted to conductivity (S/cm) using the following equation. σ = L/ R x A, where σ is conductivity in S/cm, L is the length of the sample (cm), R is resistance (Ω) and A is cross-section area (cm^2) (width x thickness) [48]. Among synthesized materials, C-POP-O shows a higher conductivity of 3.85 S/cm compared to C-POP-S (2.17 S/cm), POP-S (1.85 S/cm) and POP-O (1.29 S/cm). This is further evidence of the higher electrochemical performance of C-POP-O. In addition, the Bode phase angle plot has been included with impedance data. The Bode diagrams of the C-POP-O and C-POP-S show a lower phase angle compared to POP-O and POP-S, indicating an improvement in the charge transfer process [49], which was attributed to the carbonization process. Among carbonized POPs, C-POP-O shows a lower phase angle, confirming the faster charge transfer process. The Bode plot data are in good agreement with the Nyquist plot, confirming the higher conductivity of C-POP-O. Thus, the obtained results reveal that the POP-based materials (POP-O and POP-S) show good electrochemical activity, and upon the pyrolysis process, the carbonized POPs show enhanced activity. Further, C-POP-O exhibits superior activity due to its high conductivity and well-ordered carbon structure.

The electrochemical results suggest that C-POP-O exhibits superior catalytic activity compared to other materials. This could be due to the formation of well-ordered graphitic carbon as observed from Raman spectra. In addition, C-POP-O develops layered fragments, suggesting a more ordered, graphitic-like structure compared with other materials. This ordered structure provides a higher electrochemically active surface area as observed from CV curves and facilitates the electron transfer suggested by EIS analysis. Thus, the electrochemical and structural characterization confirms that owing to the formation of well-ordered graphitic carbon, C-POP-O is superior to other samples.

4 Conclusions

This study comprehensively analyzed the structural, morphological, and electrochemical properties of POP-O, POP-S, and their carbonized forms (C-POP-O and C-POP-S). XRD patterns revealed that both POP-O and POP-S possess an amorphous structure, while the carbonization process induces short-range graphitic domains and increased structural order. Raman analysis confirmed the formation of graphitic carbon. Further, FE-SEM images confirmed significant morphological changes post-carbonization, with C-POP-O exhibiting layered fragments and C-POP-S displaying an agglomerated morphology. Electrochemical analysis demonstrated that carbonized materials showed significant enhancement in conductivity, current density, and specific capacitance. C-POP-O exhibited a higher specific capacitance of 47.43 F g^{-1} at 1 A g^{-1} with excellent GCD cyclic stability, by retaining 96% capacitance from its starting capacitance after 5000 GCD cycles. Hence, C-POP-O displayed a strong potential as an electrode material for supercapacitor application, owing to its exceptional performance. Thus, the results obtained reveal that the carbonized POP materials, derived from POPs, can be a strong candidate as an electrode material in supercapacitors.

Supplementary Information

The online version contains supplementary material available at https://doi.org/10.1007/s42452-025-08005-x.

Supplementary material 1.

Acknowledgements

The authors gratefully acknowledge the American University of Sharjah, Materials Research Center, and Department of Biology, Chemistry and Environmental Sciences for supporting the laboratory work of this article.

Author contributions

Conceptualization, O.M.E.-K. and M.H.A.-S.; methodology, A.K., M.F.M. and F.A.S.; validation, O.M.E.-K., M.H.A.-S, A.K.; M.F.M and F.A.S.; formal analysis, O.M.E.-K., M.H.A.-S, A.K., M.F.M and F.A.S.; investigation, O.M.E.-K., M.H.A.-S, A.K., M.FM and F.A.S.; project administration, O.M.E.-K. and M.H.A.-S.; supervision, O.M.E.-K. and M.H.A.-S.; writing—original draft, A.K. M.FM and F.A.S.; writing—review and editing, O.M.E.-K. and M.H.A.-S. All authors have read and agreed to the published version of the manuscript.

Funding

This research was funded by the American University of Sharjah under grant number PDFA25-S07 and supported by the MSE Postdoctoral Fund (1127/121005). The work presented in this paper was supported, in part, by the Open Access Program from the American University of Sharjah. This paper represents the opinions of the authors and does not mean to represent the position or opinions of the American University.

Data availability

The datasets used and analyzed during the current study are available from the corresponding author on reasonable request.

Declarations

Ethics approval and consent to participate

Not applicable.

Consent for publication
Not applicable.

Competing interests
The authors declare no competing interests.

Received: 31 August 2025 / Accepted: 14 November 2025
Published online: 29 December 2025

References

1. Omer AM. Energy, environment and sustainable development. Renew Sustain Energy Rev. 2008;12:2265–300. https://doi.org/10.1016/j.rser.2007.05.001.
2. Armstrong RC, Wolfram C, De Jong KP, et al. The frontiers of energy. Nat Energy. 2016;1:1–8. https://doi.org/10.1038/nenergy.2015.20.
3. Sikiru S, Oladosu TL, Amosa TI, et al. Hydrogen-powered horizons: transformative technologies in clean energy generation, distribution, and storage for sustainable innovation. Int J Hydrogen Energy. 2024;56:1152–82. https://doi.org/10.1016/j.ijhydene.2023.12.186.
4. Muzaffar A, Ahamed MB, Hussain CM. Green supercapacitors: latest developments and perspectives in the pursuit of sustainability. Renew Sustain Energy Rev. 2024;195:114324. https://doi.org/10.1016/j.rser.2024.114324.
5. Soni N, Singh PK, Mallick S, et al. Advancing sustainable energy: exploring new frontiers and opportunities in the green transition. Adv Sustain Syst. 2024;2400160:1–23. https://doi.org/10.1002/adsu.202400160.
6. Yu Z, Kamran HW, Amin A, et al. Sustainable synergy via clean energy technologies and efficiency dynamics. Renew Sustain Energy Rev. 2023;187:113744. https://doi.org/10.1016/j.rser.2023.113744.
7. Wang S, Wasif Zafar M, Vasbieva DG, Yurtkuran S. Economic growth, nuclear energy, renewable energy, and environmental quality: investigating the environmental Kuznets curve and load capacity curve hypothesis. Gondwana Res. 2024;129:490–504. https://doi.org/10.1016/j.gr.2023.06.009.
8. Abubakr M, Elahi E, Rehman S, et al. Innovations in self-powered nano-photonics of emerging and flexible two-dimensional materials. Mater Today Phys. 2023;39:101285. https://doi.org/10.1016/j.mtphys.2023.101285.
9. Molaiyan P, Bhattacharyya S, dos Reis GS, et al. Towards greener batteries: sustainable components and materials for next-generation batteries. Green Chem. 2024;26:7508–31. https://doi.org/10.1039/d3gc05027k.
10. Dissanayake K, Kularatna-Abeywardana D. A review of supercapacitors: Materials, technology, challenges, and renewable energy applications. J Energy Storage. 2024;96:112563. https://doi.org/10.1016/j.est.2024.112563.
11. Njema GG, Ouma RBO, Kibet JK. A review on the recent advances in battery development and energy storage technologies. J Renew Energy. 2024;2024:1–35. https://doi.org/10.1155/2024/2329261.
12. Rashid Khan H, Latif Ahmad A. Supercapacitors: overcoming current limitations and charting the course for next-generation energy storage. J Ind Eng Chem. 2024;141:46–66. https://doi.org/10.1016/j.jiec.2024.07.014.
13. Girirajan M, Bojarajan AK, Pulidindi IN, et al. An insight into the nanoarchitecture of electrode materials on the performance of supercapacitors. Coord Chem Rev. 2024;518:216080. https://doi.org/10.1016/j.ccr.2024.216080.
14. Raza S, Hayat A, Bashir T, et al. Electrochemistry of 2D-materials for the remediation of environmental pollutants and alternative energy storage/conversion materials and devices, a comprehensive review. Sustain Mater Technol. 2024;40:e00963. https://doi.org/10.1016/j.susmat.2024.e00963.
15. Asadi F, Bond B, Mahata C, et al. Surface passivation on precipitated Ti-containing multi-principal element alloy subject to metal aging. Results Surf Interfaces. 2025;18:100405. https://doi.org/10.1016/J.RSURFI.2024.100405.
16. Asadi F, Paredes M. Corrosion sensors used for structural health monitoring of offshore vessels and tanks. SNAME 29th Offshore Symp TOS 2024. 2024. https://doi.org/10.5957/TOS-2024-003.
17. Chen J, Du C, Zhang Y, et al. Constructing porous organic polymer with hydroxyquinoline as electrochemical-active unit for high-performance supercapacitor. Polym (Guildf). 2019;162:43–9. https://doi.org/10.1016/j.polymer.2018.12.030.
18. Mohamed MG, Zhang X, Mansoure TH, et al. Hypercrosslinked porous organic polymers based on tetraphenylanthraquinone for CO2 uptake and high-performance supercapacitor. Polym (Guildf). 2020;205:122857. https://doi.org/10.1016/j.polymer.2020.122857.
19. Ajmal Z, Ali H, Ullah S, et al. Use of carbon-based advanced materials for energy conversion and storage applications: recent development and future outlook. Fuel. 2024;367:131295. https://doi.org/10.1016/j.fuel.2024.131295.
20. Saleh TA. A review on the technologies for converting biomass into carbon-based materials: sustainability and economy. Bioresour Technol Rep. 2024;25:101771. https://doi.org/10.1016/j.biteb.2024.101771.
21. Maqsood MF, Zubair MAA, Raza MA, et al. Fabrication and characterization of graphene oxide and glass fiber-based hybrid epoxy composites. Polym Compos. 2022;43:8072–83. https://doi.org/10.1002/pc.26952.
22. Ahmed I, Lee HJ, Jhung SH. Porous carbon derived from covalent organic frameworks and relevant porous polymers: Preparation and application in adsorption and catalysis. Chem Eng J. 2024;499:156148. https://doi.org/10.1016/j.cej.2024.156148.
23. Naz N, Manzoor MH, Naqvi SMG, et al. Porous organic polymers; an emerging material applied in energy, environmental and biomedical applications. Appl Mater Today. 2024;38:102198. https://doi.org/10.1016/j.apmt.2024.102198.
24. Shi Y, Wang Y, Meng N, Liao Y. Photothermal conversion porous organic polymers: Design, Synthesis, and applications. Small Methods. 2024;2301554:1–26. https://doi.org/10.1002/smtd.202301554.
25. Sharma A, Eadi SB, Noothalapati H, et al. Porous materials as effective chemiresistive gas sensors. Chem Soc Rev. 2024;53:2530–77. https://doi.org/10.1039/d2cs00761d.
26. Hu D, Jia Y, Yang S, et al. Redox-active 2D porous organic polymers for high-performance supercapacitor. J Ind Eng Chem. 2023;123:320–9. https://doi.org/10.1016/j.jiec.2023.03.049.
27. Xu L, Liu R, Wang F, et al. In-situ synthesis of porous organic polymer on rGO for high-performance capacitive energy storage. J Energy Storage. 2019;25:6–11. https://doi.org/10.1016/j.est.2019.100873.

28. Mondal S, Ruidas S, Chongdar S, et al. Sustainable porous heterogeneous catalysts for the conversion of biomass into renewable energy products. ACS Sustain Resour Manag. 2024;1:1672–704. https://doi.org/10.1021/acssusresmgt.4c00190.
29. Sun F, Wu D, Gao J, et al. Graphitic porous carbon with multiple structural merits for high-performance organic supercapacitor. J Power Sources. 2020;477:228759. https://doi.org/10.1016/J.JPOWSOUR.2020.228759.
30. Zang S, Jiang J, An Y, et al. A novel porous organic polymer-derived hierarchical carbon for supercapacitors with ultrahigh energy density and durability. J Electroanal Chem. 2020;876:114723. https://doi.org/10.1016/J.JELECHEM.2020.114723.
31. Tan L, Tan B. Hypercrosslinked porous polymer materials: design, synthesis, and applications. Chem Soc Rev. 2017;46:3322–56. https://doi.org/10.1039/C6CS00851H.
32. Vilela F, Zhang K, Antonietti M. Conjugated porous polymers for energy applications. Energy Environ Sci. 2012;5:7819–32. https://doi.org/10.1039/c2ee22002d.
33. Liang J, Xiao Z, Gao Y, et al. Ionothermal strategy towards template-free hierarchical porous carbons for supercapacitive energy storage. Carbon N Y. 2019;143:487–93. https://doi.org/10.1016/j.carbon.2018.11.065.
34. Sabri MA, Sara Z, Al-Sayah MH, et al. Simultaneous adsorption and reduction of cr(Vi) to cr(iii) in aqueous solution using nitrogen-rich aminal linked porous organic polymers. Sustain. 2021;13:1–13. https://doi.org/10.3390/su13020923.
35. Racik KM, Guruprasad K, Mahendiran M, et al. Enhanced electrochemical performance of MnO 2 /NiO nanocomposite for supercapacitor electrode with excellent cycling stability. J Mater Sci Mater Electron. 2019;30:5222–32. https://doi.org/10.1007/s10854-019-00821-3.
36. Bhosale R, Bhosale S, Sankannavar R, et al. Bimetallic MnFe2-MOF and its derived MnFe2O4 nanostructures for supercapacitive applications. ACS Appl Nano Mater. 2024;7:4078–91. https://doi.org/10.1021/acsanm.3c05645.
37. Muslu E, Eren E, Oksuz AU. Research progress on flexible WO3 based thin film electrodes for supercapacitor applications: a comprehensive review. Springer International Publishing; 2024.
38. Larichev YV, Yeletsky PM, Yakovlev VA. Study of silica templates in the rice husk and the carbon-silica nanocomposites produced from rice husk. J Phys Chem Solids. 2015;87:58–63. https://doi.org/10.1016/j.jpcs.2015.07.025.
39. Kumari P, Kareem A, Jhariat P, et al. Phase purity regulated by Mechano-Chemical synthesis of Metal-Organic frameworks for the electrocatalytic oxygen evolution reaction. Inorg Chem. 2023;62:3457–63. https://doi.org/10.1021/acs.inorgchem.2c03609.
40. Kim G, Ryu I, Yim S. Retarded saturation of the areal capacitance using 3D-Aligned MnO2 thin film nanostructures as a supercapacitor electrode. Sci Rep. 2017;7:1–9. https://doi.org/10.1038/S41598-017-09039-X;TECHMETA.
41. Yan W, Ayvazian T, Kim J, et al. Mesoporous manganese oxide nanowires for High-Capacity, High-Rate, hybrid electrical energy storage. ACS Nano. 2011;5:8275–87. https://doi.org/10.1021/NN2029583.
42. Helseth LE. The nonlinearities in the galvanostatic charging curves of supercapacitors provide insights into charging mechanisms. J Energy Storage. 2022;55. https://doi.org/10.1016/j.est.2022.105440.
43. Sidhu NK, Rastogi AC. Electrochemical performance of supercapacitors based on carbon nanofoam composite and microporous poly(3, 4-ethylenedioxythiophene) thin film asymmetric electrodes. Mater Chem Phys. 2016;176:75–86. https://doi.org/10.1016/j.matchemphys.2016.03.028.
44. Momodu D, Sylla NF, Mutuma B, et al. Stable ionic-liquid-based symmetric supercapacitors from capsicum seed-porous carbons. J Electroanal Chem. 2019;838:119–28. https://doi.org/10.1016/J.JELECHEM.2019.02.045.
45. Subramani K, Sudhan N, Karnan M, Sathish M. Orange Peel derived activated carbon for fabrication of High-Energy and High-Rate supercapacitors. ChemistrySelect. 2017;2:11384–92. https://doi.org/10.1002/SLCT.201701857.
46. Boujibar O, Ghamouss F, Ghosh A, et al. Activated carbon with exceptionally high surface area and tailored nanoporosity obtained from natural anthracite and its use in supercapacitors. J Power Sources. 2019;436. https://doi.org/10.1016/j.jpowsour.2019.226882.
47. Lazanas AC, Prodromidis MI. Electrochemical impedance spectroscopya tutorial. ACS Meas Sci Au. 2023;3:162–93. https://doi.org/10.1021/acsmeasuresciau.2c00070.
48. Ding Y, Zheng Z. Stretchable ionics: how to measure the electrical resistance/impedance. Matter. 2022;5:2570–3. https://doi.org/10.1016/J.MATT.2022.08.007.
49. de Araújo GM, Codognoto L, Simões FR. Self-assembled electrodes based on polyaniline grafted with reduced graphene oxide and polystyrene sulfonate. J Solid State Electrochem. 2020;24:1857–66. https://doi.org/10.1007/S10008-020-04517-1/TABLES/1.

Publisher's note